


## Mechanical and microstructural characteristics of underwater friction stir welded AA 6061-T6 joints using a hybrid GRA-artificial neural network approach

Kiran Wakchaure , Ajaykumar Thakur 

Sanjivani College of Engineering, Kopergaon, (SPPU Pune) Maharashtra, 423603, India

 [kiran.wakchaure@yahoo.com](mailto:kiran.wakchaure@yahoo.com)

**Abstract.** In this paper hybrid grey relations analysis (GRA) and an artificial neural network (ANN) are applied to study the influence of process parameters on the mechanical properties of friction stir welded aluminum alloy 6061-T6. Thirty experiments were performed by varying tool rotation speed, tool traverse speed, and tool tilt angle to study their effects on ultimate tensile strength, yield strength, percentage elongation, and impact strength of FSW joints. GRA was used to convert all responses into the single response variable, i.e., the grey relation grade (GRG). A feed-forward backpropagation ANN with two hidden layers composed of 9 and 7 neurons each was used to simulate the weld joint characteristics in terms of GRG. ANOVA analysis was used to study the influence of process parameters on grey relation grade. It was found that tool rotation speed has a significant impact on weld characteristics, followed by traverse speed and tilt angle. Based on the results it was revealed that tool rotation speed contributes 39.89% to the mechanical properties of underwater friction stir welding of AA 6061-T6, followed by tool traverse speed and tool tilt angle, respectively, by 29.87% and 19.59%. The tensile test demonstrates that the underwater FSW joint is approximately 8% stronger than the conventional air FSW joint due to grain refinement and increased nugget zone hardness because of less heat exposure and absorption.

**Keywords:** microstructure, underwater friction stir welding, artificial neural network, grey relation analysis, ANOVA

**Citation:** Wakchaure K, Thakur A. Mechanical and microstructural characteristics of underwater friction stir welded AA 6061-T6 joints using a hybrid GRA-artificial neural network approach. *Materials Physics and Mechanics*. 2023;51(1): 119-141. DOI: 10.18149/MPM.5112023\_11.

### Introduction

Friction stir welding (FSW) was developed and patented by the Welding Institute (TWI) in 1991. Earlier, it was limited to laboratory experiments to weld high-strength aluminum alloys (2xxx and 6xxx), which have limited weldability using fusion welding processes [1]. Since FSW is a solid-state welding process, it avoids defects like gas porosity, solidification cracking, residual stresses, weakening of HAZ and nugget zones, reduced corrosion resistance, etc., developed during traditional welding processes [1-2]. FSW is essentially a constrained extrusion process controlled by the non-consumable profiled tool. The tool shoulder constraints softened material, so it cannot escape easily. The material is gradually swept around the probe between the retreating side of the tool and the surrounding material as the tool traverses the joint line. Extruded material forms solid-phase joints behind the tool.

The asymmetrical joint is caused by the extrusion of the deformed material past the RS of the tool [1-3].

This process generates a significant strain and strain rate compared to other solid-state metalworking processes such as rolling, extrusion, and forging. The key parameters affecting weld quality in this welding process are tool geometry, plunging depth, rotational speed, traverse speed, and tool tilt angle [1-3]. In the AA6XXX series, 6061-T6 is a moderately strong heat-treatable alloy containing Al-Mg-Si as its primary alloying element. The  $Mg_2Si$  sediments are responsible for strengthening the AA6061 alloy. This material's high strength-to-weight ratio and corrosion resistance make it ideal for fabricating lightweight structures [5]. AA6061 possesses excellent welding characteristics but suffers a loss in strength due to the dissolution of strengthening precipitates and softening of HAZ. Friction stir welding refines the grain in the nugget zone and improves mechanical properties compared to other welding processes.

Thermal cycle and material flow behavior determine the FSW joint's microstructure evolution and mechanical properties, which are affected by process variables like rotation speed, welding speed, and tool geometry [6]. A fracture of the weld occurred along the LHZs. The tensile strength of the weld increased with increasing welding speed and was independent of tool dimension and rotation speed. Li et al. [7] reported UW-FSW of CNT/Al-Cu-Mg composites reach 94.7% efficiency when compared to FSW. The thermal cycle of underwater trials decreases, and fewer flash faults occur, which facilitates post-weld processing and increases welding productivity.

Underwater or submerged friction stir welding (UFSW/ SFSW) has become a cutting-edge welding technique that offers better mechanical properties while avoiding the welding flaws in traditional FSW [8–10]. During underwater friction stir welding, the entire welding process is carried out in the presence of water. Hofmann et al. [11] proposed using water as a cooling medium to produce ultra-fine grains in the nugget zone of friction stir processed AA6061-T6. As a result of water cooling, Wang et al. [12] found that underwater FSW of spray-formed 7075 Al alloy improves tensile properties and corrosion resistance and reduces the corrosion rate. Compared to conventional FSW, M. Hosseini et al. [13] found underwater friction stir welding to enhance the tensile strength and yield strength of ultrafine-grained AA1050. Furthermore, UFSW was proposed as a method for hardening materials on the surface. According to Rathinasuriyan et al. [14], SFSW requires more torque and power than conventional friction stir welding. Additionally, these values increase as the water head increases during submerged friction stir welding.

Bagheri et al. [15] reported numerical analyses of friction stir welding (FSW) in the air and underwater using smoothed particle hydrodynamics and finite element modelling. Underwater welding results in a lower peak temperature than traditional welding due to its higher cooling impact. In addition, peak temperature and strain rate decreased under both welding conditions as welding speed increased. Abdollahzadeh et al. [16] found that underwater FSW of 60621 T6 significantly reduced the joint temperature. This resulted in a refined microstructure in the stir zone, which improved the welded joint's mechanical properties. UFSW joints have a higher hardness than CFSW joints due to the refined grains' synergetic effect, decreased dissolution of  $\beta''$  precipitates, and fast cooling rate (intensified local deformation). SFSW of AA6061 T6 tensile strength increased with tool rotation speed and decreased with welding speed [17]. Fratini et al. [18] investigated the effects of in-process cooling within normal air, forced air, and water on the mechanical properties of friction stir welding for AA7075-T6. Results show that water is a more powerful cooling medium, improving joint tensile strength due to narrowing the weakest TMAZ and HAZ. FSW samples with water as a cooling medium show increasing microhardness values and low hardness values in the nugget zone of the water FSW sample compared with natural air and forced air

FSW samples. Sharma et al. [19] studied the effects of liquid nitrogen, regular air, and compressed air on the FSW of AA7039. During welding, cooling absorbs the excess heat, which restricts grain growth in the nugget zone and coarsens it in the HAZ. Water was also found to be the best cooling medium for maximum tensile strength and percentage elongation than compressed air and liquid nitrogen. Sinhar et al. [20] found that FSW joints with water cooling show improved yield strength, tensile strength, hardness in HAZ, and corrosion resistance due to more refined microstructure and limited precipitate restrictions as compared with conventional FSW with natural air cooling. Mahto et al. [21] reported that FSW AA6061-T6 and AISI304 form re-crystallized and deformation-textured grains in the SZ, which ultimately transform into dominant shear-and deformation-textured grains in water and air, respectively.

Abbasi et al. [22] evaluated the formability characteristics of tailor-welded blanks created by combining AA6061 aluminum alloy sheets of various thicknesses and devising friction stir vibration welding (FSVW). The results showed that FSVW-ed blanks exhibited better mechanical and formability characteristics than FSW-ed blanks. According to Abbasi et al. [23], grain size decreases from approximately 57  $\mu\text{m}$  for friction stir welding to approximately 34  $\mu\text{m}$  for friction stir vibration welding and approximately 23  $\mu\text{m}$  for underwater friction stir welding. Underwater friction stir welding and friction stir vibration welding effectively reduce precipitation size and interparticle distance. The underwater friction stir welding processed samples have the highest strength and ductility compared to friction stir welding processed samples. The cylindrical and conical tool pins used in FSW are simple in shape and easy to manufacture. Conical pin tools have better mechanical properties than cylindrical, square, and pin tools.

Multiobjective optimization is one of the elements of research in manufacturing processes. Several researchers used AHP, TOPSIS [23-25], and GRA [26-30] for the multiobjective optimization of FSW. The use of empirical non-analytical models, such as Artificial Neural Networks (ANNs), can be an effective alternative in manufacturing problems characterized by complex relationships among variables and unknown relationships among variables [22]. The usefulness of artificial neural networks has been demonstrated in metal forming, fusion welding, and machining [32]. Thapliyal et al. [33] proposed a machine-learning model to predict the ultimate tensile strength of friction stir-welded copper specimens. The result shows that ANN can predict UTS with 94% accuracy. Using five different neural networks, Manvatkar et al. [34] calculated tool and workpiece temperatures, torque, traverse force, and stresses according to the thickness of the plate, welding speed, rotating tool speed, shoulder, pin, and pin length, and the tool material for the friction stir welding. Both experimental and numerical methods were used to evaluate the performance of all ANNs. Ghetiya et al. [35] predicted the tensile strength of FSWed aluminum alloy AA8014. ANN was used to study the influence of welding parameters such as axial force, welding speed, rotational tool speed, and tool shoulder diameter on joint strength. In their study of friction stir lap welding of the Al-Mg and CuZn34 alloys, Shojaeefard et al. [36] developed an ANN model to analyze the relationship between the mechanical properties and the process parameters. Ansari et al. [37] predicted the average grain size of Magnesium ingot under friction stir extrusion processing with the effect of rotational speed, vertical speed, and extrusion hole size (HS) using a 3-6-1 artificial neural network.

Buffa et al. [38] predicted microstructure and microhardness values using ANN for the nugget zone of a Ti-6Al-4V titanium alloy FSW joint. Laubscher et al. [39] proposed a single-layer backpropagation ANN with RSM for predicting friction-welded titanium joint tensile strength based on ANN architecture 3-10-1 and sensitivity analysis. Patel et al. [40] have developed a cellular automata finite element – artificial neural network (CAFE-ANN) hybrid model to predict grain size and yield strength evolution during friction stir welding.

Maleki et al. [41] predicted tensile and hardness properties of the welding zone of FSWed AA-7075-T6 considering input parameters as the rotational and welding speed, pin diameter, shoulder diameter, axial force, and tool hardness as input parameters using ANN.

Since the submerged FSW is gaining a lot of interest nowadays, optimizing the process parameters of submerged FSW for better results would be more critical. In this research, grey relation analysis (GRA) was chosen along with an artificial neural network for the multiobjective optimization and selection of optimum process parameters. FSW is a complex welding mechanism; obtaining all the required responses for a particular set of input parameters is challenging. Hence, it is desired to use a multiobjective decision-making technique to solve this problem. Four output parameters were selected, such as yield strength, ultimate tensile strength, % elongation, and impact strength for the multiobjective optimization of underwater FSW of AA6061-T6. ANOVA analysis was carried out to determine the influence of process parameters on the mechanical properties of the welded joint.

### Methods and materials

The research was carried out on rolled plates of aluminum alloy AA 6061-T6 of 6 mm thickness. A conical tool with an 18 mm shoulder diameter and a pin with a 6 mm diameter, 14° semi-cone angle, and 5.6 mm length were considered to manufacture the tool. The chemical composition and mechanical properties of AA 6061-T6 are shown in Table 1 and Table 2, respectively. Aluminum alloy sheets were cut into sample sizes of 200(L)×75(W)×6(T)mm with an abrasive cutting machine. Edges are machined with a milling machine, and an edge of 200 mm in length, cut to a transverse direction rolling line, was considered to form a weld. Plates were washed with acetone to avoid contamination during the welding procedure. In order to manufacture the tool, a conical tool with a shoulder diameter of 18 mm and a pin diameter of 6 mm, a semi-cone angle of 14°, and a length of 5.6 mm was considered. Hot work dies steel (AISI-H13) was used as a tool material with hardening of 50-55 HRC. The main constituents of the chemical composition of H13 are C-0.4, Mn-0.4, Si-1, Mo-1.35, Cr-0.25, V-1, and Fe-balance (all elements in wt.%). A new fixture was developed to carry out welding trials, which can hold the workpiece properly and withstand the load acting on it. A special vessel-type arrangement was made with an acrylic sheet to store water in the fixture.

**Table 1.** Chemical Composition of AA6061-T6 Alloy

Elements	Mg	Si	Mn	Zn	Fe	Cu	Al
Alloying elements (in %)	1.1	0.6	0.12	0.25	0.35	0.3	Rest

**Table 2.** Mechanical properties of AA6061-T6 Alloy

Properties	UTS	YS	E	% el	$\mu$	MP	H	D
Values	303 MPa	240 MPa	68.9 GPa	20%	0.33	582–652°C	107HV	2.7 g/cc

All the experiments were carried out on a universal milling machine (G. DUFOUR make) 624D model having a vertical spindle attachment with DRO. The machine consists of the main spindle motor of 15 HP with a spindle speed range of between 24-1180 rpm. There are also two feed motors with 5 HP power, with a feed in the range of 22-1180 mm/min. The experimental setup of underwater friction stir welding is shown in Fig. 1. The Friction Stir welding tool is mounted with a collet on the spindle of a universal milling machine. The fixture was rigidly mounted on the bed of the milling machine. Specimens to be welded were

fixed in the slot made in a fixture with clamps to avoid lateral and transverse movement of specimens during trials. Firstly, the rotating tool shoulder is allowed to touch the top surface of the specimen, and then water is allowed to pour into the fixture vessel to make a 30 mm water head. An arrangement was made to pour and drain hot water from the vessel. At a distance of 14 mm from either side of the weld line and 100 mm from the start point, K-type thermocouples were employed.

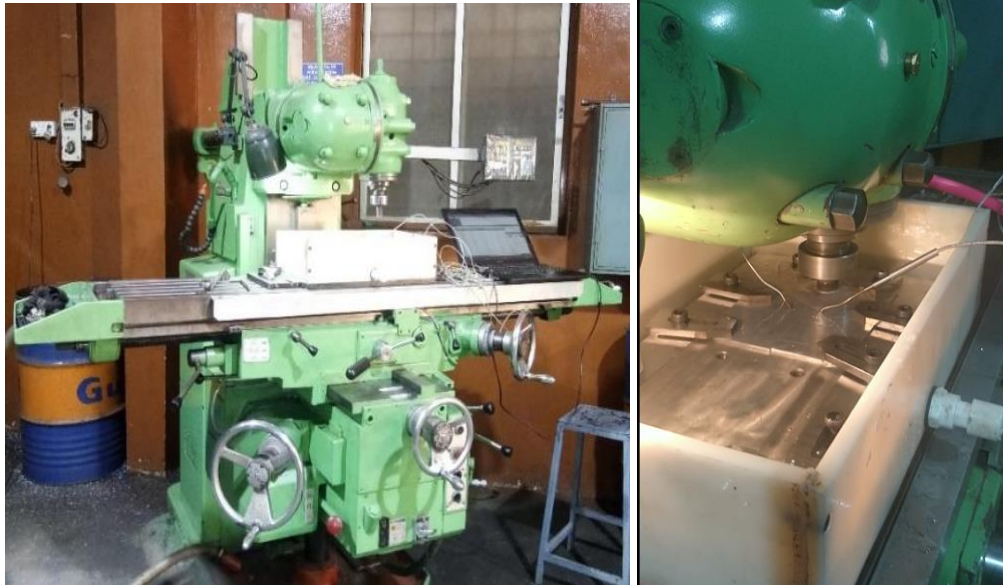


**Fig. 1.** Experimental setup

In this research, rotation speed, welding speed, and tilt angle were chosen as process parameters. Initial trials were performed to derive levels of process parameters by considering defects in the weld zone shown in Table 3.

**Table 3.** Process parameters levels

Parameter (Notation)	Unit	Level					
Tool rotation speed (TRS)	rpm	710		900		1180	
Welding speed (WS)	mm/min	22	29	49	64	83	108
Tilt Angle (TA)	° degree	1°		2°		3°	

The specimens welded with the underwater FSW procedure are shown in Fig. 2 (a) and (b) of final experimentation by considering different levels of process parameters. A total of 30 trials (shown in Table 4) were performed to analyse the effects of process parameters.

After welding trials, all welded samples were cut into the required size per the American Society for Testing of Materials (ASTM) E-8M-08 [ASTM-2008] guidelines using an abrasive water jet machine shown in Figs. 2 and 3. In this study, three samples of tensile strength, one for each impact strength, microstructure, and microhardness, were considered for the characterization. Tensile tests were performed on a 2000KN universal testing machine (UTM) (Make: Universal Motion Inc, Model: MUTCS-20 model). During tensile testing, a crosshead speed of 1 mm/min of UTM was chosen. Selected samples were considered for macro and microstructure evaluation. Optical microscopy has been carried out using a light optical microscope (Make: Conation technologies) with an image analysis system.

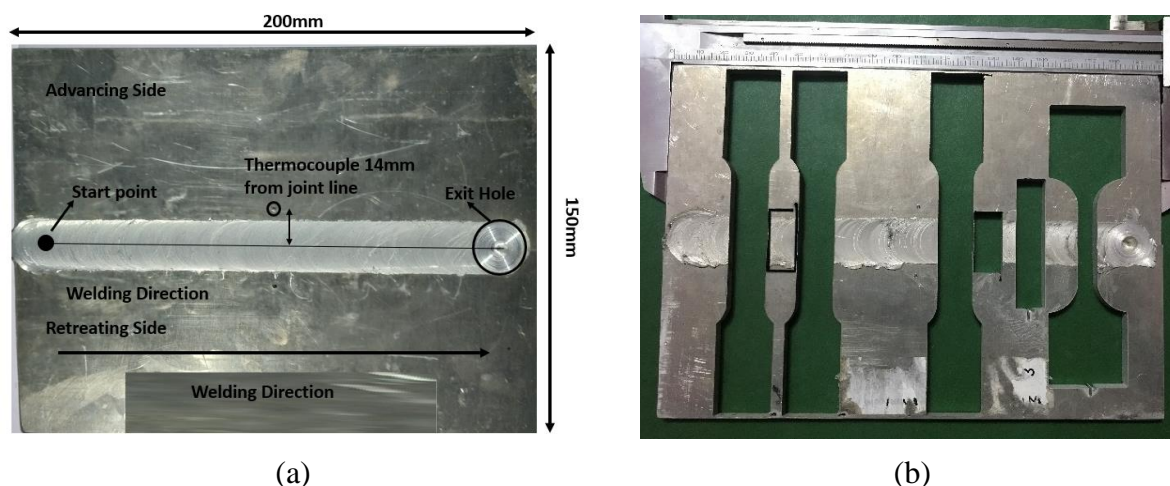
**Table 4.** Grey relation analysis

Sr. No.	Input Parameter			Output Parameters				Normalized Inputs			Normalized Responses				GR G	Rank
	TRS	TT S	TT A	UTS	% El	YS	IS	RP M	WS	TA	UT S	% El	YS	IS		
1	710	22	2	186.56	14.28	105.97	21.76	0.00	0.00	0.50	0.21	0.97	0.32	0.83	0.63	8
2	710	29	2	222.01	7.50	140.26	18.48	0.00	0.08	0.50	0.76	0.20	1.00	0.59	0.65	3
3	710	49	2	174.89	9.37	104.18	24.10	0.00	0.31	0.50	0.03	0.41	0.28	1.00	0.55	16
4	710	64	2	208.94	13.68	123.43	14.09	0.00	0.49	0.50	0.56	0.91	0.66	0.26	0.59	11
5	710	83	2	212.81	11.56	108.69	12.73	0.00	0.71	0.50	0.62	0.66	0.37	0.16	0.50	26
6	710	108	2	172.77	5.78	109.55	10.52	0.00	1.00	0.50	0.00	0.00	0.39	0.00	0.36	30
7	710	22	1	182.22	12.84	97.75	22.23	0.00	0.00	0.00	0.14	0.81	0.15	0.86	0.56	14
8	710	29	1	195.00	9.50	101.00	15.85	0.00	0.08	0.00	0.34	0.43	0.22	0.39	0.44	29
9	710	83	3	210.75	11.12	115.41	13.86	0.00	0.71	1.00	0.59	0.61	0.50	0.25	0.50	25
10	710	108	3	219.05	12.96	102.24	15.46	0.00	1.00	1.00	0.72	0.82	0.24	0.36	0.55	15
11	900	22	2	185.85	13.28	90.12	22.47	0.40	0.00	0.50	0.20	0.86	0.00	0.88	0.58	13
12	900	29	2	198.51	12.03	110.98	18.95	0.40	0.08	0.50	0.40	0.72	0.42	0.62	0.53	20
13	900	49	2	202.06	9.84	95.07	16.85	0.40	0.31	0.50	0.46	0.47	0.10	0.47	0.45	28
14	900	64	2	213.22	11.87	117.06	12.96	0.40	0.49	0.50	0.63	0.70	0.54	0.18	0.52	22
15	900	83	2	217.36	13.43	128.49	15.46	0.40	0.71	0.50	0.69	0.88	0.77	0.36	0.64	6
16	900	108	2	237.05	12.62	140.00	12.57	0.40	1.00	0.50	1.00	0.78	0.99	0.15	0.76	1
17	900	83	1	219.92	10.75	136.46	17.78	0.40	0.71	0.00	0.73	0.57	0.92	0.53	0.64	5
18	900	108	1	232.12	12.84	130.00	12.12	0.40	1.00	0.00	0.92	0.81	0.80	0.12	0.67	2
19	900	49	3	199.07	11.75	110.76	15.46	0.40	0.31	1.00	0.41	0.68	0.41	0.36	0.49	27
20	900	64	3	210.36	13.03	125.41	15.55	0.40	0.49	1.00	0.58	0.83	0.70	0.37	0.59	12
21	1180	83	2	218.28	10.62	129.06	19.89	1.00	0.71	0.50	0.71	0.56	0.78	0.69	0.62	9
22	1180	64	2	208.33	11.81	121.35	16.39	1.00	0.49	0.50	0.55	0.69	0.62	0.43	0.55	17
23	1180	49	2	204.58	10.56	115.28	17.78	1.00	0.31	0.50	0.49	0.55	0.50	0.53	0.51	24
24	1180	29	2	196.19	12.37	111.81	23.63	1.00	0.08	0.50	0.36	0.76	0.43	0.97	0.63	7
25	1180	22	2	188.12	13.43	97.89	18.25	1.00	0.00	0.50	0.24	0.88	0.16	0.75	0.53	21
26	1180	108	2	222.52	12.09	138.00	11.30	1.00	1.00	0.50	0.77	0.72	0.95	0.06	0.65	4
27	1180	49	1	207.16	12.13	106.30	16.62	1.00	0.31	0.00	0.54	0.73	0.32	0.45	0.52	23
28	1180	64	1	206.48	12.43	114.83	16.78	1.00	0.49	0.00	0.52	0.76	0.49	0.46	0.54	19
29	1180	22	3	188.93	13.00	91.23	21.06	1.00	0.00	1.00	0.25	0.83	0.02	0.78	0.54	18
30	1180	29	3	198.54	14.50	117.69	15.46	1.00	0.08	1.00	0.40	1.00	0.55	0.36	0.61	10

For metallographic investigation of welded specimens, a cross-section was taken as they were polished using various grids and etched using Tucker's reagent. Friction stir-welded specimens were polished with emery sheets of various grades. These samples were then etched for 20 seconds with Keller's reagent. EBSD and optical microscopy (OM) were used to



examine these etched specimens. EBSD is a scanning electron microscopy-based microstructural-crystallographic characterization technique used frequently to study crystalline or polycrystalline materials. All the microstructure samples were polished to different grades of emery paper followed by a diamond paste of 1  $\mu\text{m}$  particle size to evolve different zones of the welded specimen SZ, TMAZ, HAZ, and base material. Microhardness testing was carried out on the Vickers Microhardness tester of (Economet make) VH-1MD. The middle of the weld zone (transverse to weld direction) was considered a testing area with a 1mm interval using a 100g indentation load. The sub-size specimen was considered for the Charpy impact test as per ASTM E23 standards.



(a) (b)  
**Fig. 2.** Underwater friction stir welded specimen

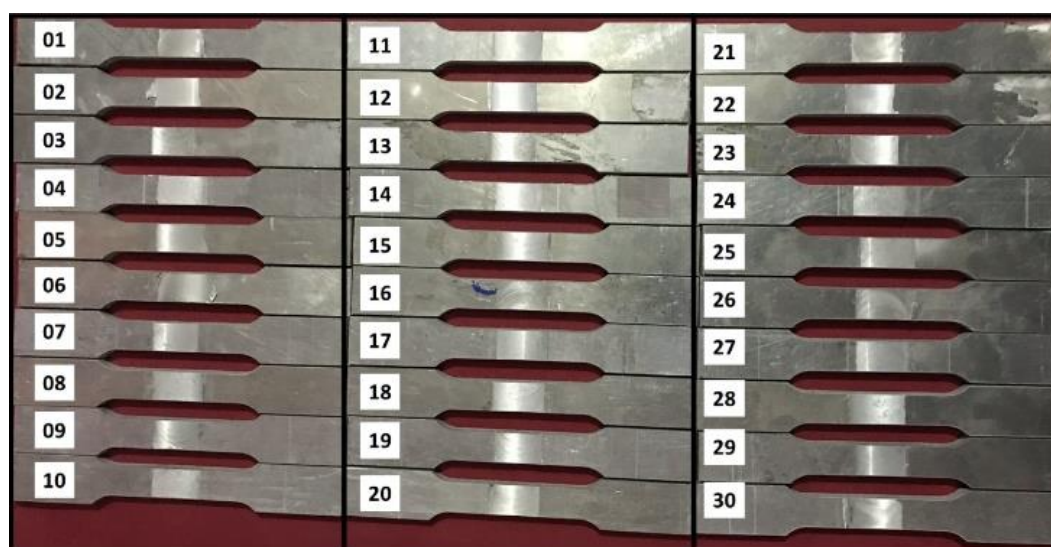


**Fig. 3.** Tensile test specimens as per E-8M-08 [ASTM-2008] guidelines

**Grey relation analysis.** Grey relation analysis is a multi-criteria decision-making technique founded by Chinese professor Julong Deng in the 1980s. GRA is an effective tool for solving inter-relationships among multiple responses and criteria. In GRA, multiple responses are converted into a single grey relation grade, which is convenient for decision-making. GRA gives the appropriate, good solution instead of the best solution for complex real-life problems. Normalization, generation of grey relation coefficient (GRC), and generation of grey relation grade (GRG) are three critical steps in GRA. In normalization, responses are normalized between values 0 to 1 according to three different performance

characteristics – the "larger the better," "smaller the better," and the "nominal the better." In this research, all the response variables, ultimate tensile strength, yield strength, impact strength, and percent elongation, should be at their maximum. Hence, all the variables were normalized with larger performance characteristics (Ref. Eq. 1). Then, the normalized data were turned into a grey relation coefficient (Ref. Eq.2) to show the relationship between the actual data and the data that was wanted. In the last step (Ref. Eq.3), an overall grey relation grade is calculated by averaging weighed grey relation coefficients.

The steps followed in the GRA are shown below:

**Step 1. Normalization** [18-20]

$$x_i^*(k) = \frac{x_i^0(k) - x_i^0(k)}{\max x_i^0(k) - x_i^0(k)}, \quad (1)$$

where  $x_i^*(k)$  is the sequence after the data preprocessing,  $x_i^0(k)$  is the reference sequence,  $x_i^0(k)$  is the smallest value in the reference sequence,  $\max x_i^0(k)$  is the largest value in the reference sequence,  $i = 1, 2, \dots, m$ ;  $k = 1, 2, \dots, n$ ;  $m$  is the number of experiments, and  $n$  is the number of experimental data.

**Step 2. Grey relation coefficient** [18-20]

$$\xi(x_0^*(k), x_i^*(k)) = \frac{\Delta_{\min}(k) + \zeta \Delta_{\max}(k)}{\Delta_{0i}(k) + \zeta \Delta_{\max}(k)}, \quad (\text{Table 5. C16-C19}) \quad (2)$$

$$\Delta_{0i}(k) = \|x_0^*(k) - x_i^*(k)\|, \quad (2.1)$$

$$\Delta_{\min}(k) = \min_{j \in i} \min_{\forall k} \|x_0^*(k) - x_j^*(k)\|,$$

$$\Delta_{\max}(k) = \max_{j \in i} \max_{\forall k} \|x_0^*(k) - x_j^*(k)\|,$$

where  $\Delta_{0i}(k)$  is the deviation sequence of the comparability sequence  $x_i^*(k)$  and reference sequence  $x_0^*(k)=1$ ,  $\zeta$  is the distinguishing coefficient, having a value between 0-1. The value of 0.5 is generally used.

**Step 3. Grey relation grade** [18-20]

$$\gamma_i(x_0^*(k), x_i^*(k)) = \frac{1}{n} \sum_{i=1}^n w_i \xi(x_0^*(k), x_i^*(k)), \quad (3)$$

where  $w_i$  is the weighting value of the  $i^{\text{th}}$  performance characteristic, and here 0.25 is the weight considered for each response variable,  $\gamma_i(x_0^*(k), x_i^*(k))$  is the GRG for an  $i^{\text{th}}$  experiment, and  $n$  is the number of performance characteristics.

First, using Eq. (1), the experimental data consisting of process parameters and responses have been normalized. Tensile strength, yield strength, elongation percentage, and impact strength were evaluated using the largest-the-better (LB) criterion. Based on Eq. (2), grey relational coefficients are calculated for each performance characteristic with weights of  $w_1 = 0.5$  and  $w_2 = 0.5$  [13]. Eq. 3 has been used to calculate the grey relational coefficients for each response. FSW quality is measured by the grey relational grade, a comprehensive measure. GRA transforms the multi-response optimization problem into a single optimization problem with equivalent objective functions. The GRG is the relationship between the reference sequence values and comparability sequence values.

Table 10 indicates the optimal factor combination with a high GRG value. A tool rotation of 900 rpm, a tilt angle of 2 degrees, and a welding speed of 108 mm/min are the optimal conditions for the FSW of aluminum alloy. Table 5 shows the network topology and training parameters of the ANN to GRG, and Table 6 shows each level's mean grey relational grade ratio according to the process parameters. Table 7 shows the absolute error values for different neural networks.

**An artificial neural network (ANN).** An artificial neural network (ANN) is a computational network inspired by biological processes. ANNs are optimization techniques that use data analysis and simulation to model the human brain or neural system. The main benefits of ANNs are that they can access more data and remove noise and insufficient data. ANNs are advantageous because of their calculation speed, ability to learn from examples and



simplicity. Due to these characteristics, ANNs can be applied to materials science. FSW responses have been modeled and predicted by several researchers using ANNs. Manvatkar et al. [36] used a feed-forward network and the backpropagation algorithm for various combinations of welding variables to generate tool durability maps to study tool strength.

Networks are multi-layered, with an input layer for parameters, an output layer for the response, and a hidden layer for processing input using a training function. Four input neurons were used to develop neural networks. In each hidden layer, 1-10 neurons were used to train the data, and one neuron predicted the mechanical properties of welded joints. Input layer nodes represent tool rotation speed, transverse tool speed, and tool tilt angle, which are used to predict response. After training several networks, the number of hidden layers and neurons in each layer was determined. In this study, back propagation neural network with three neurons for the input parameters and one neuron for the response of FSW in terms of grey relation grade.

The training functions "logsig" and "tansig" are used in the first and second hidden layers, respectively. An ANN model was trained with 70% of the readings, validated with 15%, and tested with 15%. A linear regression analysis was also performed between the ANN outputs (predictions) and the corresponding targets (experiments) to evaluate the ANN-based model response. After several trials, the model was developed with two hidden layers containing 1-10 neurons each. A network with minimum absolute relative error and maximum correlation coefficient criteria was used to select the required neural network by training and validating several neural networks. The absolute relative error was calculated with the root to mean square (RSM) error shown in Eq. 4 and the correlation coefficient shown in Eq 5. Neurons in hidden layers one and two were validated with "logsig" and "tagsig" activation functions.

$$\text{Absolute Relative Error} = |RMSE_{Train} - RMSE_{Val}|, \quad (4)$$

$$\text{where } RMSE_{Train} = \left[ \left( \frac{1}{p} \right) \sum_j |t_j - o_j|^2 \right]^{\frac{1}{2}}; \quad RMSE_{Val} = \left[ \left( \frac{1}{p} \right) \sum_j |t_j - o_j|^2 \right]^{\frac{1}{2}}.$$

$$R^2 = 1 - \left[ \frac{\sum_j (t_j - o_j)^2}{\sum_j (o_j)^2} \right]^{\frac{1}{2}}. \quad (5)$$

Network parameters used to train and validate the networks as shown in Table 5.

**Table 5.** Network topology and training parameters of the ANN to GRG

Network parameter	Content
Number of input nodes	3
Number of hidden layers	2
Number of output nodes	1
Number of neurons for each hidden layer	Layer1=9, Layer 2=7
Network type	Feed forward back propagation
Training function	Levenberg–Marquardt
Transfer functions for hidden layers	logsig, tansig
Transfer functions for the output layer	Linear
Performance function	MSE
Training epoch	300
Goal	0.0001

One hundred neural networks were tested with varying neurons in two hidden layers to select the optimal neuron sets in hidden layers. Tables 6 and 7 show that the network with nine neurons in hidden layer 1 and 7 neurons in hidden layer 2 shows the highest correlation

coefficient ( $R^2$ ) is 0.9937, and the slightest absolute error of 0.0021. Hence to train the neural networks, 3-9-7-1 architecture was chosen to predict the grey relation grade.

**Table 6.** Correlation coefficient ( $R^2$ ) for different neural networks

		Layer 2									
Layer 1	Neurons	1	2	3	4	5	6	7	8	9	10
	1	0.6892	0.6636	0.7017	0.4764	0.5315	0.3679	0.6266	0.5031	0.4530	0.6986
	2	0.6760	0.8289	0.6192	0.5921	0.4645	0.6688	0.9691	0.3169	0.5352	0.8687
	3	0.6336	0.7232	0.6495	0.5406	0.9110	0.9875	0.6857	0.6252	0.7901	0.8351
	4	0.9159	0.7816	0.7183	0.5610	0.4624	0.8267	0.6953	0.6191	0.1319	0.5056
	5	0.5753	0.7340	0.6174	0.8097	0.5934	0.6564	0.9065	0.6930	0.6009	0.5936
	6	0.7000	0.8581	0.5812	0.6299	0.9627	0.8522	0.9475	0.6644	0.4279	0.7815
	7	0.7254	0.5310	0.9679	0.6704	0.6573	0.5874	0.9704	0.7635	0.8179	0.5863
	8	0.9436	0.6040	0.5583	0.9227	0.1089	0.8556	0.9184	0.8283	0.7068	0.8041
	9	0.6561	0.8712	0.6353	0.9200	0.6328	0.6823	<b>0.9909</b>	0.9229	0.6204	0.8194
	10	0.8391	0.5643	0.8690	0.9664	0.7029	0.7514	0.9739	0.9806	0.8580	0.8990

**Table 7.** Absolute error values for different neural networks

		Layer 2									
Layer 1	Neurons	1	2	3	4	5	6	7	8	9	10
	1	0.0919	0.0448	0.1190	0.0270	0.1665	0.0578	0.1156	0.0027	0.1484	0.0208
	2	0.1063	0.1749	0.0695	0.1246	0.0651	0.0365	0.0045	0.0319	0.2044	0.1449
	3	0.1275	0.1495	0.0238	0.1930	0.0949	0.0068	0.0499	0.0390	0.2084	0.0310
	4	0.1157	0.0546	0.0417	0.0105	0.1068	0.1738	0.0186	0.0106	0.1169	0.0634
	5	0.0879	0.1094	0.0643	0.1512	0.1244	0.1236	0.0283	0.0403	0.0051	0.0219
	6	0.0834	0.0791	0.0424	0.1089	0.1388	0.1687	0.0640	0.0774	0.2137	0.0062
	7	0.1249	0.0500	0.0131	0.1532	0.1820	0.1360	0.1810	0.0912	0.0024	0.0849
	8	0.1581	0.1281	0.1286	0.1541	0.1032	0.1588	0.2424	0.2220	0.0438	0.1972
	9	0.1207	0.2402	0.1194	0.0733	0.0999	0.1003	<b>0.0021</b>	0.0445	0.2045	0.2543
	10	0.0739	0.0097	0.0481	0.1634	0.0511	0.1650	0.0753	0.2281	0.0588	0.0960

The experimental results and neural network predictions of the process parameters follow each other very closely shown in Table 8, so the developed ANN can accurately predict the grey relation grade. Consequently, it is possible to achieve overall performance without performing any experiments. A neural network model could forecast outcomes better if its mean squared error is lower.

For the GRG, the correlation coefficients were 0.9833, 0.9884, and 0.9938 at the training, validation, and testing stages, respectively shown in Fig. 4. The percentage relative error between the trained and the predicted value by ANN were closely matched, and the maximum percentage of errors was about 3.7% which is within the acceptable level. The low relative error values and average absolute relative error in FSW, as well as the strong correlation coefficients between predicted and experimental results, demonstrate the outstanding capability of artificial neural networks to model mechanical properties without requiring a priori knowledge of thermal and material flow, microstructural and mechanical analysis.

**Table 8.** ANN predictions

Sr. No	1	2	3	4	5	6	7	8	9	10
GRG	0.6268	0.6531	0.5526	0.5944	0.4960	0.3624	0.5623	0.4350	0.5035	0.5544
ANN Pred	0.6492	0.6289	0.5458	0.6073	0.4871	0.3579	0.5566	0.4424	0.4870	0.5609
Error	0.0223	0.0241	0.0067	0.0130	0.0089	0.0044	0.0057	0.0074	0.0166	0.0065
% Error	3.6%	3.7%	1.2%	2.2%	1.8%	1.2%	1.0%	1.7%	3.3%	1.2%
Sr. No	11	12	13	14	15	16	17	18	19	20
GRG	0.5766	0.5308	0.4507	0.5240	0.6359	0.7647	0.6440	0.6656	0.4928	0.5912
ANN Pred	0.5785	0.5248	0.4523	0.5102	0.6503	0.7654	0.6408	0.6665	0.4839	0.5963
Error	0.0019	0.0060	0.0017	0.0138	0.0144	0.0006	0.0032	0.0008	0.0088	0.0051
% Error	0.3%	1.1%	0.4%	2.6%	2.3%	0.1%	0.5%	0.1%	1.8%	0.9%
Sr. No	21	22	23	24	25	26	27	28	29	30
GRG	0.6172	0.5462	0.5104	0.6291	0.5271	0.6491	0.5166	0.5421	0.5434	0.6053
ANN Pred	0.6276	0.5456	0.5183	0.6179	0.5313	0.6504	0.5231	0.5492	0.5518	0.5954
Error	0.0104	0.0005	0.0079	0.0112	0.0042	0.0013	0.0065	0.0071	0.0084	0.0099
% Error	1.7%	0.1%	1.5%	1.8%	0.8%	0.2%	1.3%	1.3%	1.5%	1.6%

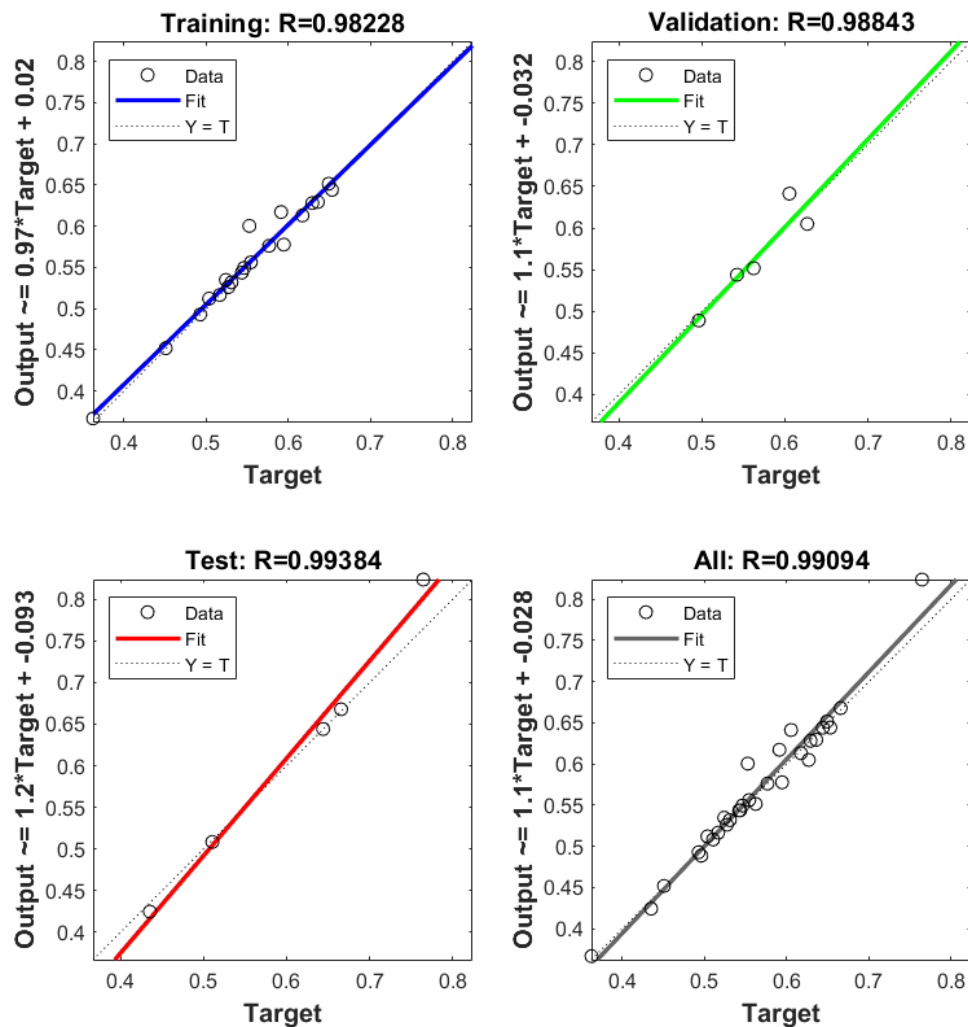


**Fig. 4.** ANN regression values

**Prediction of optimum process parameters.** To predict the optimum process parameters, trained ANN (3-9-7-1) was used. From the grey relation analysis, it was observed that 900 rpm, tool rotation speed, 108 mm/min tool traverse speed, and Tilt angle  $2^\circ$  show the highest value of grey relation grade of 0.7647 (sr. no 16 of Table 4). The same set of parameters was used to obtain the optimum process parameter by varying each parameter by keeping two parameters constant to simulate the neural network. As shown in Fig 5 (a), the effect of tool rotation speed on grey relation grade is predicted using a trained neural network by keeping 108 mm/min of TTS and tilt angle  $2^\circ$  constant. Results show that GRG value increases with an increase in tool rotation speed up to 975 rpm, then decreases.

Also, for the tool traverse speed, the grey GRG value increases with an increase in TTS for TRS 900 rpm and TTA of  $2^\circ$ , as shown in Fig. 5 (b). Maximum grey relation grade obtained at 108 mm/min. Figure 5 (c) shows GRG value increases with an increase in tool tilt angle from  $1-2^\circ$  and then decreases. Maximum grey relation grade obtained at  $2^\circ$ .

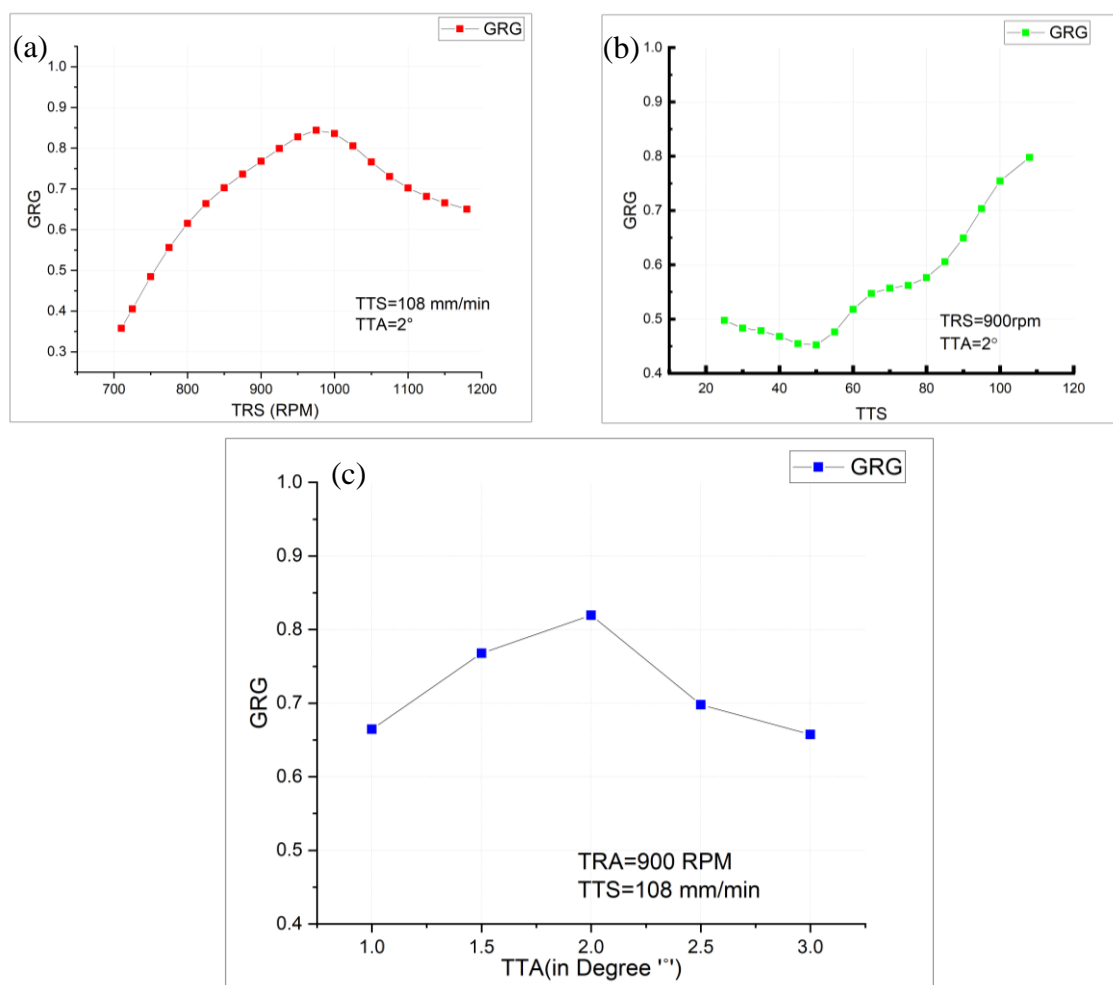


**Fig. 5.** Prediction of GRG using ANN

After simulating the results, optimum parameters predicted by the ANN are Tool rotation speed of 975 rpm, tool transverse speed of 108mm/min, and tool tilt angle of  $2^\circ$ , as shown in Table 9. The grey relation grade obtained using the proposed GRA-ANN approach was 0.8440 with revised optimum parameters tool rotation 975 rpm, tilt angle  $2^\circ$ , and welding speed 108 mm/min, a 9.32% improvement over the 0.7647 obtained experimentally at 900 rpm and 108 mm/min. The results show that the adoption of the GRA-ANN hybrid

optimization method leads to a significant improvement of mechanical properties in friction stir welding.

As the milling machine has limited settings of the tool rotation speed, 975 rpm was not possible with the machine. Hence closed match speed setting of 900 rpm was considered the optimum speed with a transverse tool speed of 108mm/min and tool tilt angle of 2°. The same parameters were used for the conventional in-air friction stir welding experiment after the optimal process parameters were determined for underwater friction stir welding. Mechanical and microscopic investigations were conducted to compare underwater and in-air FSW performance.

**Table 9.** Results of welding performance using the GRA and ANN

Method	Optimum process conditions			GRG	% Improvement in GRG
	TRS	TTS	TA		
GRA	900	108	2°	0.7647	---
GRA-ANN(Pred)	900	108	2°	0.7653	--
TAGUCHI-GRA-ANN (optimized parameters)	975	108	2°	0.8440	9.32%

### Result and discussion

**ANOVA analysis.** The grey relation grade obtained using the proposed GRA-ANN approach was 0.8440 with revised optimum parameters tool rotation 975 rpm, tilt angle 2°, and welding speed 108 mm/min, a 9.32% improvement over the 0.7647 obtained experimentally at 900 rpm and 108 mm/min. [42]. The results of the ANOVA test are shown in Table 10. In addition, a percentage contribution is calculated. In the 1920s, statistician and geneticist R.A. Fisher developed Fisher's F-distribution to test for statistical significance. In this paper, ANOVA analysis was carried out to find the % contribution of each process parameter to the mechanical properties of the welded joint. From Table 10, in ANOVA analysis, it is observed that input parameter tool rotation speed is having highest % contribution of 39.89%, followed by 29.87% and 19.59% of Tool traverse speed and Tool tilt angle, respectively on mechanical properties of underwater friction stir welding of AA 6061-T6.

**Table 10.** ANOVA analysis

Parameters	SS Value	DOF	MS Value	F-Value	P-value	% Contribution
TRS	0.0672	2	0.0336	3.743941	0.041456.	39.89%
TTS	0.1258	5	0.02516	2.803499	0.046358.	29.87%
TTA	0.033	2	0.0165	1.838543	0.188142	19.59%
Error	0.17949	20	0.008975			10.65%
Total	0.40549	29				

Increasing the rotational tool speed improves the grey relation grade to a maximum for a given TTS and TTA. The material is mixed and stirred around the pin due to frictional heating and plastic deformation caused by tool rotation speed. Insufficient tensile strength and yield strength might be caused by low heat generation and plastic deformation at low rotational speeds. On the other hand, a high rotational speed is characterized by turbulent material flow and localized softening due to the abundance of heat created. The presence of strengthening precipitates, dissolution, and coarsening, decreases the strength of the welded joint. Welds produced with tool speeds close to 900 rpm have better mechanical properties because sufficient heat is generated for effective softening and mixing of the deformed material. The strength of the joint tends to increase as welding speed increases.



**Characterization of welded joint.** Macroscopic images of all 30 samples are free from any volumetric defect except flash over the top surface of the weld. Figure 6 shows a macroscopic image of an underwater friction stir welding sample welded with optimum process parameters obtained with ANN-GRA analysis. For the micro and macrostructural investigations, specimens were processed with the optimum process, and parameters were used. For the comparative study, for the same optimum parameters, a new specimen was welded with the conventional in-air friction stir welding process. A macrograph of underwater FSW shows distinct HAZ, TMAZ, and SZ zones, whereas, for in-air FSW, the HAZ and TMAZ are separated by a thin boundary. The macrograph of the weld sample shows well-defined onion rings consisting of bright and dark field regions, which denote uniform material flow in the nugget zone shown in Fig. 6. Exposure to water in UFSW makes the weld smoother compared with FSW.

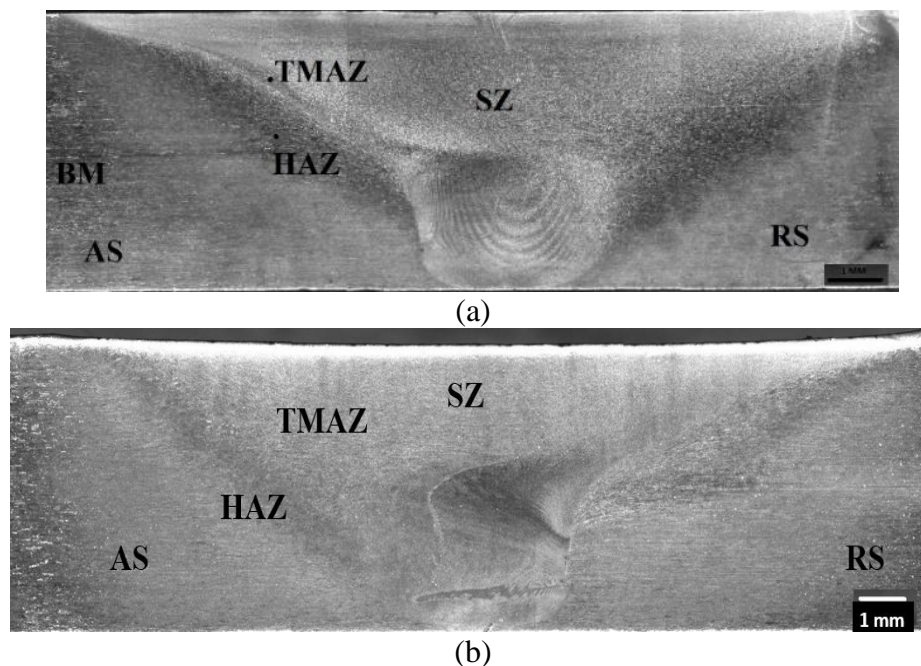


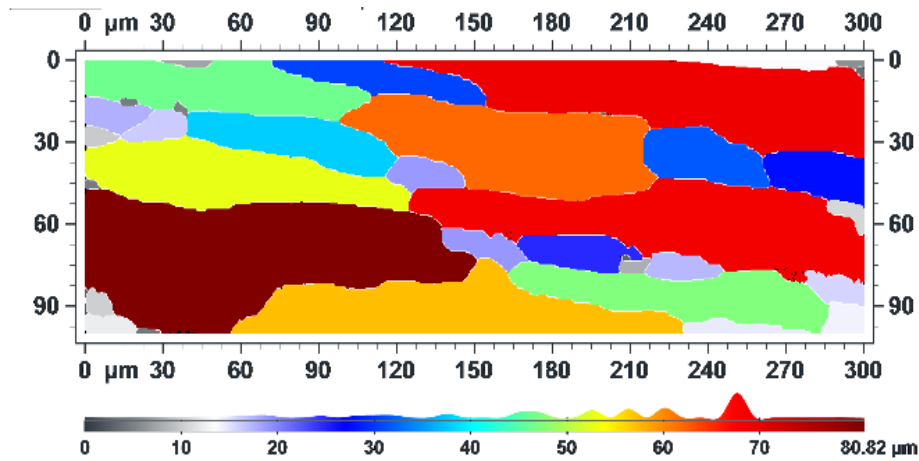
**Fig. 6.** Macroscopic image of an underwater friction stir welding sample welded with optimum process parameters

The plastic deformation generated by the FSW process severely compresses the pre-deformed coarse grains, resulting in the creation of extremely fine recrystallized equiaxed grains within the weld nugget. In addition, the dynamic recrystallisation (DRX) phenomenon, which is theoretical to have been induced by the adsorption of dislocations by sub-grain boundaries, may have also aided in the nucleation and development of ultrafine grains in the FSW weld nugget. As grain refinement takes place, which precedes to increase of microhardness ultimately increases the tensile strength of the joint due to water as a cooling medium carrying out heat from the weld specimens rapidly. This rapid cooling is responsible for restricting grain growth, which leads to refined grains in the weld nugget zone. Slight variation in the grain size of FSW welded samples of both the condition shows that the cooling effect due to water dominates the development of tool pin profiles with the same process parameters. Further, the microstructure analysis the specimen welded in water analysed using EBSD techniques.

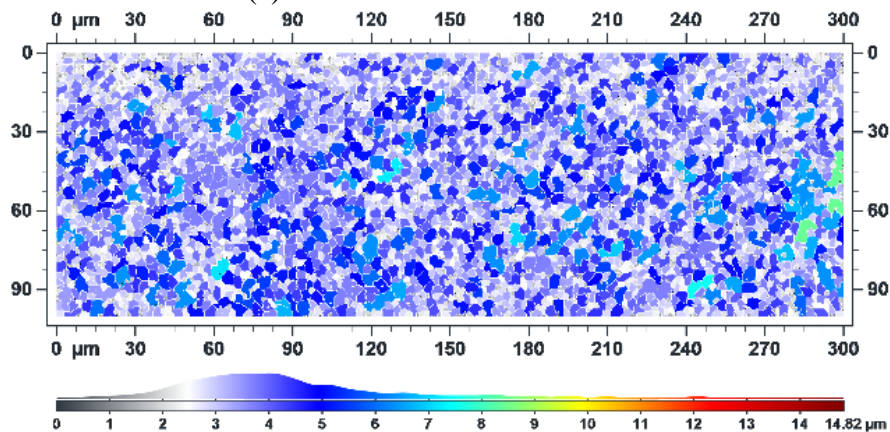
Figure 7 shows the EBSD grain maps of base metal compared with the weld nugget zone of UFSW and CFSW analysed using the ATEX software tool [23]. Figure 7 (a) shows the EBSD maps of base material and which shows elongated grains with an average 84  $\mu\text{m}$

grain size. Figures 7 (b) and 7 (c) shows the components and grains map of TMAZ prepared under water and in air. Where, slightly more refined grains of size  $2.56 \mu\text{m}$  were observed for water as compared with the air. It was because of effective heat distribution and plastic deformation that occurred due to water which refine grains in the welding zone compared with the air.

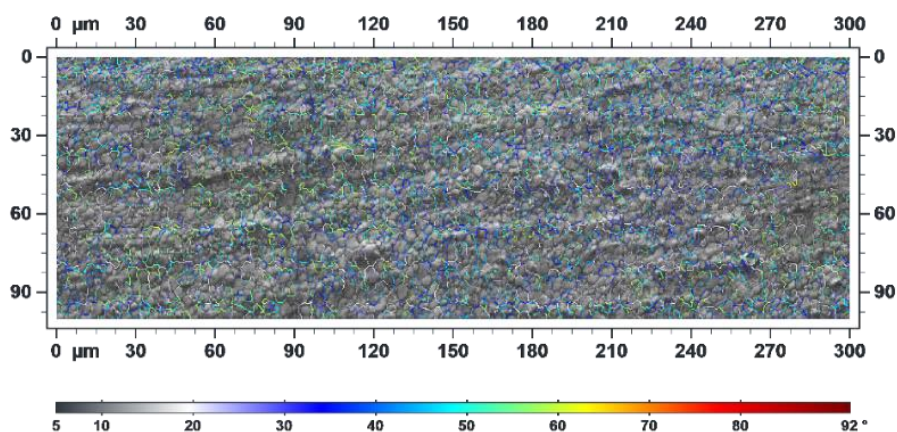
In FSW, the base material of  $84 \mu\text{m}$  grain size undergoes severe plastic deformation, and grain refinements provide an equiaxed grain size. The average grain size in UFSW is  $2.65 \mu\text{m}$ , and the CFSW is  $4.91 \mu\text{m}$ . The water environment in UFSW restricted grain growth in the nugget zone after processing, providing finer grain UFSW compared with CFSW. Due to the shear deformation generated by the rotating tool, the parent grains tend to be reoriented along the flow pattern around the pin, which is a characteristic of TMAZ. Observation of newly-formed equiaxed grains indicates the presence of dynamic recrystallization (DRX). From the exterior to the interior of the TMAZ, there is a trend for more equiaxed grains to develop. With closer proximity to the core of the weld, higher temperatures and more locational deformation are obtained, resulting in an increase in DRX. The texture transition happens on the TMAZ border. The alterations are concentrated in a small area. This region also has significant diversity in grain size.



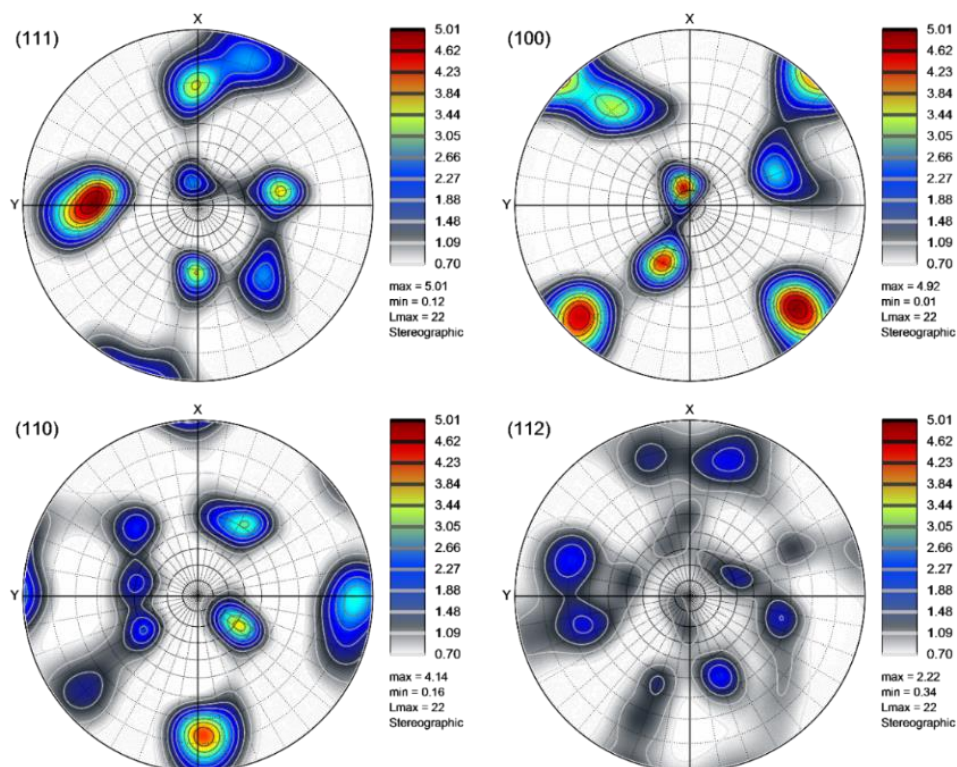
(a) Grain structure of base material



(i) EBSD maps of FSW specimen prepared underwater

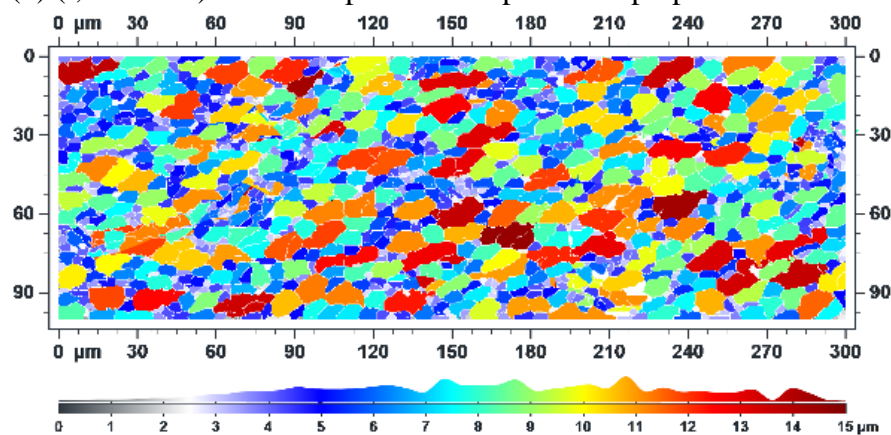


(ii) EBSD maps showing grain boundaries for underwater FSW



(iii) Pole maps of underwater FSW

(b) (i, ii and iii) EBSD maps of FSW specimens prepared underwater



(i) EBSD maps of FSW specimen prepared in air



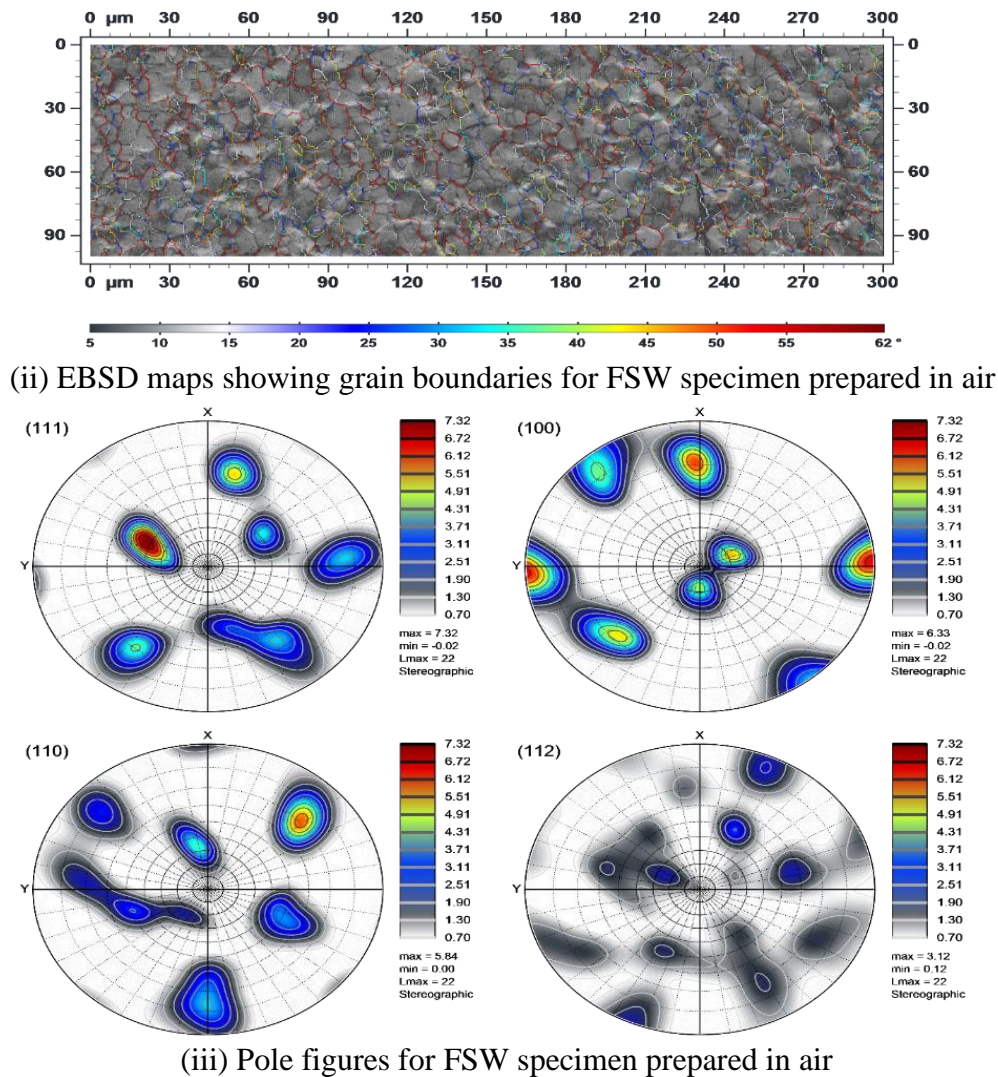


**Fig. 7.** EBSD Maps of a) base metal, b) Underwater FSW, c) In air FSW

In FSW, due to intense recrystallization because of stir action, grain refinement occurs which is responsible for changing mechanical properties in a welded joint. Underwater friction stir welding reduces the thermal exposure in nugget zone, which restricts grain growth due to natural aging during the cooling of the joint, which adds extra benefit to improve the mechanical properties of the joint. The grain refining process is driven by grain subdivision at the cooler perimeter of the tool's deformation zone and the geometric effects of strain, which reduce the overall high-angle border spacing with increasing deformation. Nevertheless, it also involves thermally induced high-angle grain boundary migration, which increases as the temperature approaches the tool. The later, higher-temperature stages of the refining process resemble geometric dynamic recrystallisation. As a result of static annealing in the thermal wake of the tool, the nugget grain structure becomes more equiaxed and coarsens slightly, as well. As indicated previously, sites with relatively large deformation stresses exhibit discontinuous recrystallization; yet, continuous recrystallization is also accompanied by grains refining. In the SZ, a steady change from low-angle borders to high-angle boundaries can be detected, according to studies of grains distribution in the literature [21,22].

The low angle boundaries for the specimen prepared in water are nearly 28.5 % as seen in Fig. 7 (b-ii) whereas high angle boundaries are 71.5 % with an average grain size of 3.21  $\mu\text{m}$  and texture intensity of 5.01 as observed in pole Fig. 7 (b-iii). On the other side, the

low angle boundaries for the specimen prepared in the air are nearly 25.4% as seen in Fig. 7 (c-ii) whereas, high angle boundaries are 74.6 % with an average grain size of 8.1  $\mu\text{m}$  and texture intensity of 7.32 as observed in pole Fig. 7 (c-iii).

The high temperatures and intense deformation experienced during FSW/UFSW result in different textures, precipitates dissolving, and coarsening. The macrostructure has three distinct zones: the stir zone (SZ), the TMAZ, and the HAZ. There is a distinct boundary between TMAZ/HAZ and SZ. The grains of BM are non-deformed and elongated. Typically, the SZ exhibits equiaxed and refined grains that have been dynamically recrystallized. New grains are formed in the SZ due to intensive plastic deformation caused by tool stirring and heat generated by tool rubbing. Figure 8 shows Vickers microhardness profiles measured along the midsections of base material, CFSW, and UFSW specimens. The base material has an average hardness value of 107 HV. The weld regions of HTAAs usually become soft as a result of FSW. The UFSW joints of AA6061 soften due to coarsening and dissolution of strengthening precipitates during FSW/UFSW [43].

It was observed that precipitation-hardened AAs typically have 'W' type hardness profiles (Fig. 8). The advancing side undergoes severe plastic deformation in friction stir welding compared with the retreating side. Due to this, the advancing side undergoes higher temperatures than the retreating side, reducing the region's microhardness. AS in UFSW, with low-temperature exposure in the welding region, the hardness value increases, as shown in Fig. 8. The retreating side in UFSW shows a minimum hardness of 70.2 Hv on the interface of TMAZ /HAZ. For the CFSW minimum hardness value observed in the HAZ zone of the Advancing side.

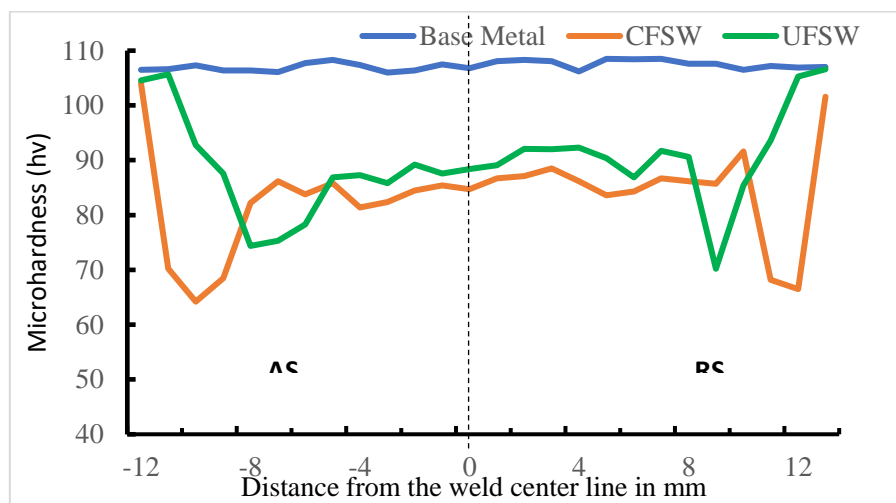


**Fig. 8.** Microhardness profile of UFSW sample

For CFSW samples, due to high heat input on AS, microhardness in AS (64-86 HV) was lower than that in RS (66-87HV). A maximum microhardness of 85 HV was found in the SZ of RS, which was lower than the average microhardness of 107 HV found in the BM. Compared to SZ, TMAZ/HAZ exhibited a noticeable decrease in microhardness. Microstructure analysis revealed that SZ contains fine grains and precipitates. Refined grains with many grain boundaries resist dislocation motion when indented or loaded. As a result, the SZ exhibits a higher microhardness than the TMAZ. There was grain growth (coarsening) in the TMAZ and HAZ. Due to a coarse boundary, there is less resistance to dislocation motion, which makes grain boundaries less available. TMAZ and HAZ have low grain boundary strengthening, contributing to their low hardness. As reported, it was found that in UFSW, TMAZ and HAZ were narrowing, which reduced softening regions in the nugget



zone [7]. TMAZ/HAZ might also have a lower hardness due to the dissolution of strengthening precipitates, Lin et al. [44] observed similar results.

The tensile test results for the base metal, underwater friction stir welding, and conventional in-air friction stir welding (CFSW) samples are shown in Fig 9. Figure 9 shows that welding speed increases from 29-108 mm/min improves mechanical properties. As a result of welding at lower speeds, high heat levels are generated, compromising the growth and dissolution of strengthening precipitates. With higher welding speeds, thermal cycles are reduced, which improves tensile strength and inhibits grain growth and precipitate dissolution. According to Liu et al. [45], the tensile strength first increases with welding speed and then dramatically decreases at 200 mm/min due to the groove defect, which is present at a fixed rotation speed of 800 rpm.

The optimal process parameters used to process both CFSW and UFSW samples are TRS 900 rpm, WS 108 mm/min, with  $TA = 2^\circ$ . Friction stir welding undergoes thermal heating, which reduces mechanical properties compared to a base metal, which results in tensile strength of 303.5 MPa and a 20% elongation. Results show underwater samples show a tensile strength of 237.25 MPa (78.17% of BM) with an elongation of 13.44% (76.08% of BM). FSW samples processed in the air (CFSW) show a tensile strength of 216.88 MPa (71.45% of BM) with an elongation of 12.5% (63.2%) of BM).

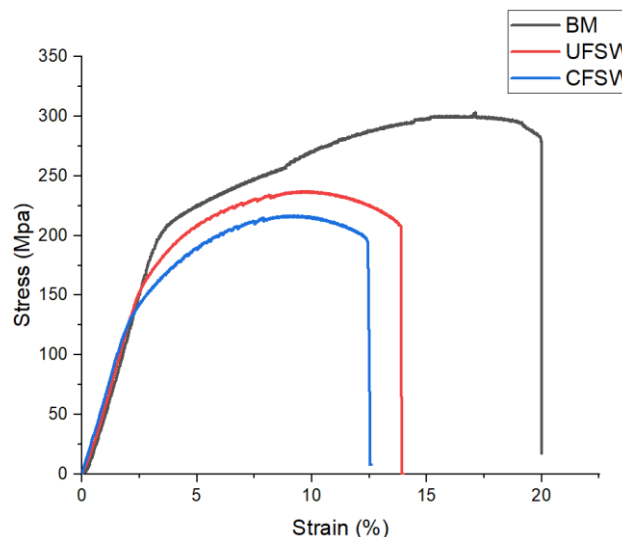


**Fig. 9.** Stress-Strain curves for BM, CFSW, and UFSW

Tensile strength was increased by 10.7% when the welding medium was changed from air to water [46]. The peak temperature in the UFSW is lower than in the FSW due to water's higher heat absorption capacity. In addition, UFSW results in a shorter dwell time above a given temperature and a lower peak temperature due to more significant heating and cooling rates [46]. Water cooling limits the coarsening and dissolution of strengthening precipitates due to reduced temperatures and less thermal gradient. As a result, an optimal underwater FSW joint may be more substantial than a conventional FSW joint.

The hardness minimum is a potential fracture location during transverse tensile loading of heat-treatable Al alloys since the hardening precipitates dominate the strength [46]. In FSW, zones with low hardness distribution are prone to fracture initiation. Figure 10 (a) shows tensile test specimens' fracture surface locations. Based on current research, CFSW tensile test fracture occurs on the AS in the HAZ adjacent to the TMAZ, which has the lowest hardness [43]. Microfractographs (Fig. 10 (b)) show some equiaxed dimples, indicating ductile fracture modes. Dawood et al. [47] attribute small dimples to homogeneous microstructures at the failure site.

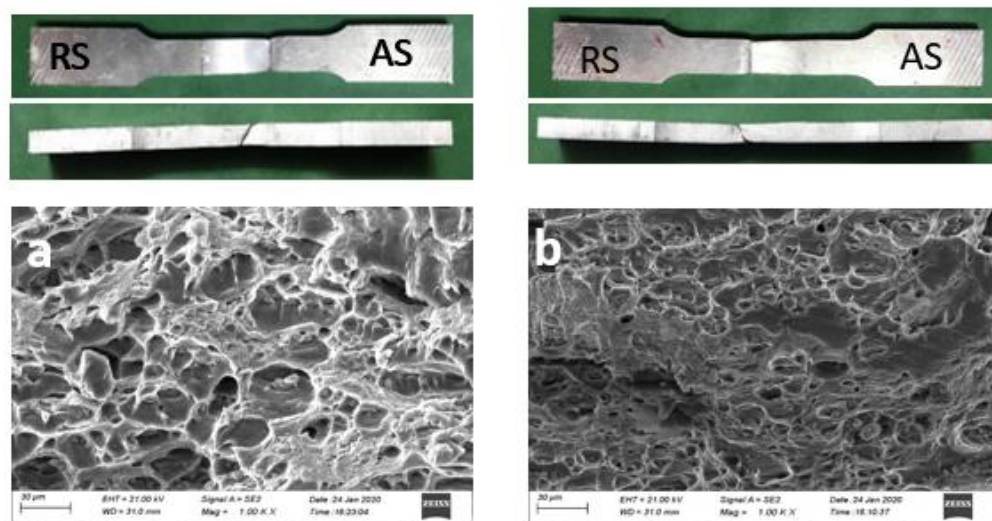


**Fig. 10.** The tensile fracture surfaces of weld joints welded a) CFSW b) UFSW

Typically, the advancing side achieves higher temperatures, causing grain growth, and resulting in the lowest hardness region. The fracture position shifts from advancing to retreating when the cooling medium changes from air to water shown in Fig. 10 (b) for UFSW, fracture occurs in the low hardness zone of the interface of TMAZ and HAZ on the retreating side [48,49]. Several large dimples are evident on the fracture surface of Figs. 10 (a) and (b), indicating significant plastic deformation during tensile testing. Joints welded in air exhibit larger and deeper dimples than joints welded in water; the fracture surfaces of the joints welded in air exhibit ductile characteristics with large dimples. In some positions on the fracture surface of the joint welded in water, there are small dimples with secondary cracks, and quasi-cleavage planes are visible [49].

## Conclusions

In the present investigations, multiobjective optimization was performed using ANN-GRA for UFSW of AA 6061-T6 aluminium alloy using a conical tool. The ultimate tensile strength, yield strength, elongation percentage, and impact strength, optimal process parameters were determined and optimized for tool rotation speed, welding speed, and tilt angle. Based on the results of this study, the following conclusions were drawn:

1. For UFSW the ANN multilayer network 3-9-7-1 shows optimum results in terms of grey relation grade with a correlation coefficient of 0.9909 and an absolute minimum error of 0.0021. In a model trained with an ANN, a grey relation grade increases with tool rotation speed as it increases from 700 to 910 rpm, then decreases. In addition, the grey relation grade increases with an increase in tool traverse speed from 22 to 108 mm/min.
2. Based on GRA-ANN, 0.8440 grey relation grades were predicted with new optimum parameters of 900 rpm, 2° tilt angle, and 108 mm/min welding speed, compared to 0.7647 obtained experimentally at 900 rpm, 2° tilt angle, and 108 mm/min.
3. ANOVA analysis revealed that tool rotation speed contributes 39.89% to the mechanical properties of underwater friction stir welding of AA 6061-T6, followed by tool traverse speed and tool tilt angle, respectively, by 29.87% and 19.59%.
4. Underwater FSW samples show the highest strength of 237.25 MPa (78.17% of BM) compared with the air (CFSW) sample of 216.88 MPa (71.45% of BM).
5. The UFSW produces refined grains in the nugget zone and thus improves the microhardness and tensile strength of the joints compared with in-air friction stir welding.

## References


1. Mishra RS, Ma ZY. Friction stir welding and processing. *Mater. Sci. Eng. R Reports*. 2005;50(1-2): 1–78.
2. Ma ZY. Friction Stir Processing Technology: A Review. *Metall. Mater. Trans. A*. 2008;39: 642–658.
3. Rai R, De A, Bhadeshia HKDH, Deb Roy T. Review: friction stir welding tools. *Sci Technol Weld Join*. 2011;16: 325–342.
4. Mishra RS, Mahoney MW. (Eds.) *Friction Stir Welding and Processing*. ASM International; 2007.
5. Zhou L, Li GH, Liu CL, Wang J, Huang YX, Feng JC, et al. Effect of rotation speed on microstructure and mechanical properties of self-reacting friction stir welded Al-Mg-Si alloy. *Int. J. Adv. Manuf. Technol*. 2017;89: 3509–3516.
6. Liu W, Shen Y, Guo C. Microstructures and mechanical properties of submerged friction stir welding of ME20M Magnesium alloy. In: *16th Int. Bhurban Conf. Appl. Sci. Technol.* IEEE; 2019. p.1–6.
7. Li X, Zhang Z, Peng Y, Yan D, Tan Z, Zhou Q, Wang K, Zhou M. Microstructure and mechanical properties of underwater friction stir welding of CNT/Al-Cu-Mg composites. *J. Mater. Res. Technol*. 2022;18: 405–415.
8. Paramaguru D, Pedapati SR, Awang M. *The Advances in Joining Technology*. Singapore: Springer; 2019.
9. Wahid MA, Khan ZA, Siddiquee AN. Review on underwater friction stir welding: A variant of friction stir welding with great potential of improving joint properties. *Transactions of Nonferrous Metals Society of China*. 2018;28(2): 193–219.
10. Rathinasuriyan C, Muniamuthu S, Mystica A, Senthil Kumar VS. Current Status and Development of Submerged Friction Stir Welding: A Review. *International Journal of Precision Engineering and Manufacturing-Green Technology*. 2021;8: 687–701.
11. Hofmann DC, Vecchio KS. Submerged friction stir processing (SFSP): An improved method for creating ultra-fine-grained bulk materials. *Mater. Sci. Eng. A*. 2005;402: 234–241.
12. Wang Q, Zhao Y, Yan K, Lu S. Corrosion behavior of spray formed 7055 aluminum alloy joint welded by underwater friction stir welding. *Mater. Des*. 2015;68: 97–103.
13. Hosseini M, Danesh Manesh H. Immersed friction stir welding of ultrafine grained accumulative roll-bonded Al alloy. *Mater. Des*. 2010;31: 4786–4791.
14. Rathinasuriyan C, Muniamuthu S, Mystica A, Senthil Kumar VS. Investigation of heat generation during submerged friction stir welding on 6061-T6 aluminum alloy. *Mater. Today Proc*. 2021;46: 8320–8324.
15. Bagheri B, Abbasi M, Abdollahzadeh A, Kokabi AH. Numerical analysis of cooling and joining speed effects on friction stir welding by smoothed particle hydrodynamics (SPH). *Arch. Appl. Mech*. 2020;90: 2275–2296.
16. Abdollahzadeh A, Bagheri B, Abassi M, Kokabi AH, Moghaddam AO. Comparison of the Weldability of AA6061-T6 Joint under Different Friction Stir Welding Conditions. *J. Mater. Eng. Perform*. 2021;30: 1110–1127.
17. Fathi J, Ebrahimzadeh P, Farasati R, Teimouri R. Friction stir welding of aluminum 6061-T6 in presence of watercooling: Analyzing mechanical properties and residual stress distribution. *Int. J. Light Mater. Manuf*. 2019;2: 107–115.
18. Fratini L, Buffa G, Shivpuri R. In-process heat treatments to improve FS-welded butt joints. *Int. J. Adv. Manuf. Technol*. 2009;43: 664–670.
19. Sharma C, Dwivedi DK, Kumar P. Influence of in-process cooling on tensile behaviour of friction stir welded joints of AA7039. *Mater. Sci. Eng. A*. 2012;556: 479–487.

20. Sinhmar S, Dwivedi DK. Enhancement of mechanical properties and corrosion resistance of friction stir welded joint of AA2014 using water cooling. *Mater. Sci. Eng. A*. 2017;684: 413–422.
21. Mahto RP, Rout M, Pal SK. Mechanism of microstructure evolution and grain growth in friction stir welding of AA6061-T6 and AISI304 in air and water media. *Mater. Chem. Phys.* 2021;273: 125081.
22. Abbasi M, Bagheri B, Abdollahzadeh A, Moghaddam AO. A different attempt to improve the formability of aluminum tailor welded blanks (TWB) produced by the FSW. *Int. J. Mater. Form.* 2021;14: 1189–1208.
23. Abbasi M, Abdollahzadeh A, Bagheri B, Ostovari Moghaddam A, Sharifi F, Dadaei M. Study on the effect of the welding environment on the dynamic recrystallization phenomenon and residual stresses during the friction stir welding process of aluminum alloy. *Proc. of the Institution of Mechanical Engineers, Part L: Journal of Materials: Design and Applications*. 2021;235: 1809–1826.
24. Velukkudi Santhanam SK, Ramaiyan S, Rathinaraj L, Chandran R. *Multi Response Optimization of Submerged Friction Stir Welding Process Parameters Using Grey Relational Analysis. Vol 2 Adv Manuf.* American Society of Mechanical Engineers; 2016.
25. Şimşek B, İç YT, Şimşek EH. A TOPSIS-based Taguchi optimization to determine optimal mixture proportions of the high strength self-compacting concrete. *Chemom. Intell. Lab. Syst.* 2013;125: 18–32.
26. Hasan M, Abdi R, Akbari M, Shojaeefard MH, Behnagh RA, Akbari M, Besharati Givi MK, Farhani F. Modelling and pareto optimization of mechanical properties of friction stir welded AA7075/AA5083 butt joints using neural network and particle swarm algorithm. *Mater. Des.* 2013;44: 190–198.
27. Lin JL, Lin CL. The use of the orthogonal array with grey relational analysis to optimize the electrical discharge machining process with multiple performance characteristics. *Int. J. Mach. Tools. Manuf.* 2002;42: 237–244.
28. Sudeepan J, Kumar K, Barman TK, Sahoo P. Mechanical and Tribological Behavior of ABS/TiO<sub>2</sub> Polymer Composites and Optimization of Tribological Properties Using Grey Relational Analysis. *J. Inst. Eng. Ser. C*. 2015;97: 41–53.
29. Hsiao YF, Tarng YS, Huang WJ. Optimization of Plasma Arc Welding Parameters by Using the Taguchi Method with the Grey Relational Analysis. *Mater. Manuf. Process.* 2007;23: 51–58.
30. Wakchaure KN, Thakur AG, Gadakh V, Kumar A. Multi-Objective Optimization of Friction Stir Welding of Aluminium Alloy 6082-T6 Using hybrid Taguchi-Grey Relation Analysis- ANN Method. *Mater. Today Proc.* 2018;5: 7150–7159.
31. Aydin H, Bayram A, Esme U, Kazancoglu Y, Guven O. Application of Grey Relation Analysis (Gra) and Taguchi Method for the Parametric Optimization of Friction Stir Welding (Fsw) Process. *Mater. Tehnol.* 2010;44: 205–211.
32. Ansari MA, Abdi Behnagh R, Lin D, Kazeminia S. Modelling of Friction Stir Extrusion using Artificial Neural Network (ANN). *Neural Computing and Applications*. 2019;31: 7211–7226.
33. Thapliyal S, Mishra A. Machine learning classification-based approach for mechanical properties of friction stir welding of copper. *Manuf. Lett. Society of Manufacturing Engineers (SME)*. 2021;29: 52–55.
34. Manvatkar VD, Arora A, De A, DebRoy T. Neural network models of peak temperature, torque, traverse force, bending stress and maximum shear stress during friction stir welding. *Sci. Technol. Weld. Join.* 2012;17: 460–466.
35. Ghetiya ND, Patel KM. Prediction of tensile strength in friction stir welded aluminium alloy using artificial neural network. *Procedia Technol.* 2014;14: 274–281.

36. Shojaeefard MH, Akbari M, Asadi P. Multi Objective Optimization of Friction Stir Welding Parameters Using FEM and Neural Network. *International Journal of Precision Engineering and Manufacturing*. 2014;15: 2351–2352.
37. Ansari MA, Abdi Behnagh R, Lin D, Kazeminia S. Modelling of Friction Stir Extrusion using Artificial Neural Network (ANN). *Int. J. Adv. Des. Manuf. Technol.* 2018;11(4): 1-12.
38. Buffa G, Fratini L, Micari F. Mechanical and microstructural properties prediction by artificial neural networks in FSW processes of dual phase titanium alloys. *J. Manuf. Process.* 2012;14: 289–296.
39. Laubscher RPIDRF. Application of an artificial neural network model to predict the ultimate tensile strength of friction - welded titanium tubes. *J. Brazilian Soc. Mech. Sci. Eng.* 2019;41: 111.
40. Patel C., Das S., Narayanan RG. CAFE modeling, neural network modeling, and experimental investigation of friction stir welding. *Proc. Inst. Mech. Eng. Part C J. Mech. Eng. Sci.* 2013;227: 1164–1176.
41. Maleki E. Artificial neural networks application for modeling of friction stir welding effects on mechanical properties of 7075-T6 aluminum alloy. *IOP Conf. Ser. Mater. Sci Eng.* 2015;103: 012034.
42. Kumar J, Majumder S, Mondal AK, Verma RK. Influence of rotation speed, transverse speed, and pin length during underwater friction stir welding (UW-FSW) on aluminum AA6063: A novel criterion for parametric control. *Int. J. Light Mater. Manuf.* 2022;5: 295–305.
43. Li D, Yang X, Cui L, He F, Shen H. Effect of welding parameters on microstructure and mechanical properties of AA6061-T6 butt welded joints by stationary shoulder friction stir welding. *Mater. Des.* 2014;64: 251–260.
44. Lin H, Wu Y, Liu S, Zhou X. Effect of cooling conditions on microstructure and mechanical properties of friction stir welded 7055 aluminium alloy joints. *Mater. Charact.* 2018;141: 74–85.
45. Liu HJ, Zhang HJ, Yu L. Effect of welding speed on microstructures and mechanical properties of underwater friction stir welded 2219 aluminum alloy. *Mater. Des.* 2011;32: 1548–1553.
46. Venkateswarulu D, Cheepu M, Krishnaja D, Muthukumaran S. Influence of Water Cooling and Post-Weld Ageing on Mechanical and Microstructural Properties of the Friction-Stir Welded 6061 Aluminium Alloy Joints. *Appl. Mech. Mater.* 2018;877: 163–176.
47. Dawood HI, Mohammed KS, Rahmat A, Uday MB. The influence of the surface roughness on the microstructures and mechanical properties of 6061 aluminium alloy using friction stir welding. *Surf. Coatings Technol.* 2015;270: 272–283.
48. Banik A, Deb Barma J, Saha SC. Effect of Threaded Pin Tool for Friction Stir Welding of AA6061-T6 at Varying Traverse Speeds: Torque and Force Analysis. *Iran J. Sci. Technol – Trans. Mech. Eng.* 2020;44: 749–764.
49. Zhao Y, Wang Q, Chen H, Yan K. Microstructure and mechanical properties of spray formed 7055 aluminum alloy by underwater friction stir welding. *Mater. Des.* 2014;56: 725–730.

## THE AUTHORS

**Kiran Wakchaure**   
e-mail: kiran.wakchaure@yahoo.com

**Ajaykumar Thakur**   
e-mail: ajay\_raja34@yahoo.com